PAPER

Structural trends in ten-vertex endohedral clusters, M@E$_{10}$ and the synthesis of a new member of the family, [Fe@Sn$_{10}$]$^{3−}$†

Tobias Krämer, Jack C. A. Duckworth, Matthew D. Ingram, Binbin Zhou, John E. McGrady* and Jose M. Goicoechea*

The synthesis of a new endohedral ten-vertex Zintl ion cluster, [Fe@Sn$_{10}$]$^{3−}$, isoelectronic with [Fe@Ge$_{10}$]$^{3−}$, is reported. In an attempt to place this new cluster within the context of the known structural chemistry of the M@E$_{10}$ family (M = transition metal, E = main group element), we have carried out a detailed electronic structure analysis of the different structural types: *viz* bicapped square antiprismatic ([Ni@Pb$_{10}$]$^{2−}$, [Zn@In$_{10}$]$^{8−}$), tetra-capped trigonal prismatic ([Ni@In$_{10}$]$^{10−}$) and the remarkable pentagonal prismatic [Fe@Ge$_{10}$]$^{3−}$ and [Co@Ge$_{10}$]$^{3−}$. We establish that the structural trends can be interpreted in terms of a continuum of effective electron counts at the E$_{10}$ cage, ranging from electron deficient (<4n + 2) in [Ni@In$_{10}$]$^{10−}$ to highly electron rich (>4n + 2) in [Fe@Ge$_{10}$]$^{3−}$. The effective electron count differs from the total valence electron count in that it factors in the increasingly active role of the metal d electrons towards the left of the transition series. The preference for a pentagonal prismatic geometry in [Fe@Ge$_{10}$]$^{3−}$ emerges as a natural consequence of backbonding to the cage from four orthogonal 3d orbitals of the low-valent metal ion. Our calculations suggest that the new [Fe@Sn$_{10}$]$^{3−}$ cluster should also exhibit structural consequences of backbonding from the metal to the cage, albeit to a less extreme degree than in its Ge analogue. The global minimum lies on a very flat surface connecting D_{4d}, C_{2v} and C_{3v}-symmetric minima, suggesting a very plastic structure that may be easily deformed by the surrounding crystal environment. If so, then this provides a new and quite distinct structural type for the M@E$_{10}$ family.

Introduction

Transition metal-centred clusters of the group 14 elements have been studied in the gas phase for many years,[1] but only relatively recently have stable analogues suitable for structural analysis been isolated.[2] For example, the 60-valence-electron‡

Department of Chemistry, Inorganic Chemistry Laboratory, University of Oxford, South Parks Road, Oxford OX1 3QR, UK. E-mail: john.mcgrady@chem.ox.ac.uk; jose.goicoechea@chem.ox.ac.uk

‡Here and elsewhere we choose to identify the clusters by their *total* valence electron count (*i.e.* cage + metal d) because this number is unambiguous and does not pre-judge the question of the participation of the metal-based electrons in cluster bonding.

†Electronic supplementary information (ESI) available: Discussion of crystallographic data and EPR spectroscopy. Kohn–Sham eigenvalue diagram (spin-α and spin-β) for the D_{4d}, C_{2v} and D_{5h}-symmetric isomers of [Fe@Ge$_{10}$]$^{3−}$ (Fig. S3). Energies and structural parameters for the D_{4d}-, C_{3v}-, C_{2v}- and D_{5h}-symmetric structures of [Ni@Pb$_{10}$]$^{2−}$, [Zn@In$_{10}$]$^{8−}$, [Fe@Ge$_{10}$]$^{3−}$ and [Fe@Sn$_{10}$]$^{3−}$ (Tables S1–S4). Optimised structural parameters of the C_2-symmetric global minimum of [Fe@Sn$_{10}$]$^{3−}$ (Fig. S4). Optimised structural parameters of vacant cages (Table S5). Cartesian coordinates and total energies of all stationary points. Complete ref. 24*c*. See DOI: 10.1039/c3dt50643f

[Pt@Pb$_{12}$]$^{2−}$ dianion was isolated by Eichhorn and co-workers from the reaction of [Pb$_9$]$^{4−}$ with [Pt(PPh$_3$)$_4$] (Ph = C$_6$H$_5$),[3] and its perfectly icosahedral structure is readily interpreted in terms of a closed-shell d^{10} Pt(0) centre encapsulated within a *closo* deltahedral cage. Indeed the icosahedral motif is common to all members of the homologous series [M@Pb$_{12}$]$^{2−}$ (M = Ni, Pd, Pt)[4] and also to the isoelectronic iridium analogue [Ir@Sn$_{12}$]$^{3−}$.[5] Our recent synthesis of a 58-electron cluster, [Mn@Pb$_{12}$]$^{3−}$,[6] the first fully characterised example of a paramagnetic M@E$_{12}$ cluster, provided some insight into the structural consequences of electron deficiency (in the sense of a reduction in the total electron count). In stark contrast to the [M@Pb$_{12}$]$^{2−}$ (M = Ni, Pd, Pt) family, the [Mn@Pb$_{12}$]$^{3−}$ unit is strongly distorted from perfectly icosahedral symmetry, adopting a prolate D_{2d}-symmetric structure. Based on a DFT analysis of the electronic structure of [Mn@Pb$_{12}$]$^{3−}$, we argued that, despite the formal electron deficiency, the distortion was driven by an accumulation of electron density on the Pb$_{12}$ cage, such that the effective electron count is *greater* than the 50 valence electrons appropriate for a *closo* cluster.[7] The 3d orbitals of Mn are far from inert, and play an active structural

role through backbonding to the vacant orbitals of the cage. The extent to which they participate in this way is strongly dependent on the effective nuclear charge, and structural distortions are predicted to be negligible in the isoelectronic later transition metal cluster $Ni@Pb_{12}$.[8]

Whilst the structural variance within the $M@E_{12}$ family is striking, it pales into insignificance compared to the $M@E_{10}$ analogues (Fig. 1, Table 1). In 2005, Eichhorn and co-workers reported a 52-electron $[Ni@Pb_{10}]^{2-}$ cluster anion which adopts a bicapped square antiprismatic structure (D_{4d}, Fig. 1a).[3,9] Unlike the $M@E_{12}$ clusters, where all M–E and E–E bonds are symmetry-equivalent in the icosahedron, a 'pseudo-spherical' reference point is harder to define in the 10-vertex case, simply because the apical and equatorial vertices are symmetry distinct. Thus in the empty *closo* $[Pb_{10}]^{2-}$ cage reported by Fässler and co-workers[10] the Pb–Pb bond lengths span a relatively narrow range (3.07 Å–3.31 Å) and this necessarily imposes very different distances between the centroid of the cluster and the apical and equatorial vertices (3.25 and 2.65 Å, respectively). This prolate bicapped square antiprism with M–E (apical) > M–E (equatorial) is therefore the structural fingerprint of a *closo* 10-vertex cage. The fact that the structure of the $[Ni@Pb_{10}]^{2-}$ cluster is strikingly similar to that of the empty cage (Pb–Pb: 3.09 Å–3.41 Å, Ni–Pb: 3.21 Å (apical), 2.72 Å (equatorial)), suggests that it can be viewed as a structurally inert d^{10} Ni(0) centre encapsulated in a *closo* ($4n + 2 = 42$ electron) $[Pb_{10}]^{2-}$ cage. An analysis of the electronic structure of

isoelectronic $[Ni@Ge_{10}]^{2-}$ by Chen *et al.* using density functional theory confirmed the absence of significant electron transfer between the d^{10} transition metal and the cage.[11] The deltahedral $[Ni@Pb_{10}]^{2-}$ cluster can therefore be regarded as the direct analogue of the $[Ni@Pb_{12}]^{2-}$ case in the twelve-vertex series, in so much as the metal 3d orbitals are inert in both cases.

More than a decade before Eichhorn's report of the structure of $[Ni@Pb_{10}]^{2-}$, Sevov and Corbett had described the structures of 50-electron $[M@In_{10}]^{n-}$ units in the alloys $K_8In_{10}Zn$ and $K_{10}In_{10}M$, M = Ni, Pd and Pt.[15] In the $[Zn@In_{10}]^{8-}$ case the structure is again approximately D_{4d}-symmetric, although now compressed along the four-fold axis, such that the apical and equatorial Zn–In distances are similar (2.84 Å, 2.82 Å) while the In–In distances vary over a wider range (3.04 Å to 3.64 Å). The isoelectronic $[Ni@In_{10}]^{10-}$ unit in $K_{10}In_{10}Ni$ is also markedly distorted compared to $[Pb_{10}]^{2-}$, and was described as approximately C_{3v}-symmetric, based on a tetra-capped trigonal prismatic architecture. The differences between the $[Zn@In_{10}]^{8-}$ and $[Ni@In_{10}]^{10-}$ units are, however, subtle, and the most striking feature is that both are significantly distorted from the natural *closo* reference point defined by $[Ni@Pb_{12}]^{2-}$ or $[Pb_{12}]^{2-}$. Extended Hückel theory offers an elegant rationalization for these distortions, suggesting that the central metal retains a d^{10} configuration ($Ni^{(0)}$, $Zn^{(II)}$) while the 40-electron $[In_{10}]^{10-}$ cage is electron deficient. The observed distortions are then driven by the need to destabilise precisely one of the occupied orbitals of the putative 42-electron *closo* $[In_{10}]^{12-}$ cage to accommodate the reduction of two in the electron count. We note here the contrast with our model for the distortions in $[Mn@Pb_{12}]^{3-}$ where the cage carries an *excess* of electron density relative to the *closo* reference point.

The structural chemistry of the 10-vertex cages took a new twist in 2009 with the concurrent reports of the structures of 51-electron $[Fe@Ge_{10}]^{3-}$,[16] and 52-electron $[Co@Ge_{10}]^{3-}$,[17] both of which adopt unprecedented pentagonal prismatic geometries (Fig. 1, D_{5h}). A number of calculations reported in the literature have established beyond doubt that these D_{5h}-symmetric structures are indeed the global minima for the two species in question. For example, Fässler and co-workers showed that the D_{5h}-symmetric structure of $[Co@Ge_{10}]^{3-}$ lies 0.58 eV below the D_{4d}-symmetric bicapped square antiprismatic alternative.[17] Moreover, the order is reversed for the isoelectronic nickel species $[Ni@Ge_{10}]^{2-}$, where the D_{4d}-symmetric structure identified by Chen is 0.23 eV *more* stable than its D_{5h}-symmetric counterpart. King and co-workers have also addressed the issue of the balance between D_{5h} and D_{4d} structural forms in endohedral clusters of the later transition elements.[18] Their calculations (B3LYP/LANL2DZ) again confirm the preference for a D_{4d}-symmetric structure in $[Ni@Ge_{10}]^{2-}$ (the D_{5h}-symmetric structure lying 0.25 eV higher at this level of theory), and also indicate that the pentagonal prism is preferred for the heavier (as yet unknown) congeners, $[Pd@Ge_{10}]^{2-}$ and $[Pt@Ge_{10}]^{2-}$.

Despite the unambiguous theoretical confirmation of D_{5h}-symmetric global minima for both $[Fe@Ge_{10}]^{3-}$ and $[Co@Ge_{10}]^{3-}$,
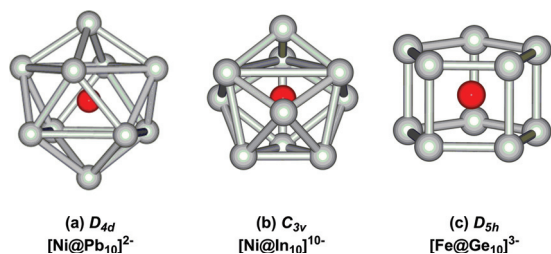

Fig. 1 Known structural motifs adopted by ten-vertex endohedral clusters: (a) bicapped square antiprismatic (D_{4d}) ($[Ni@Pb_{12}]^{2-}$), (b) tetra-capped trigonal prism (C_{3v}) ($[Ni@In_{10}]^{10-}$), (c) pentagonal prismatic (D_{5h}) ($[Fe@Ge_{10}]^{3-}$ and $[Co@Ge_{10}]^{3-}$).

Table 1 Structurally characterised ten-vertex Zintl cluster anions and their total valence electron (TVE) counts

Cluster	TVE	Point group	Ref.
$[Pb_{10}]^{2-}$	42	D_{4d}	10
$[Ni@Pb_{10}]^{2-}$	52	D_{4d}	9
$[Co@Ge_{10}]^{3-}$	52	D_{5h}	17
$[Fe@Ge_{10}]^{3-}$	51	D_{5h}	16
$[Zn@In_{10}]^{8-}$	50	D_{4d}	15
$[Ni@In_{10}]^{10-}$	50	C_{3v}	15
$[Ni@Ge_9Ni(CO)]^{2-}$	50	C_{3v}	12
$[Ni@Ge_9Ni(CCPh)]^{3-}$	50	C_{3v}	12
$[Ni@Ge_9Ni(en)]^{3-}$	51	C_{3v}	12
$[Ge_{10}Mn(CO)_4]^{3-}$	42	D_{4d}	13
$[Ge_9MR]^{3- a}$	42	D_{4d}	14

^{a} M = Zn, Cd; R = Ph, mes, ^iPr.

the underlying reasons for the adoption of a pentagonal prismatic geometry remain unclear. Based on the Mulliken population analysis, and in particular the very negative charges on the metal centers, King and co-workers argue that the clusters $[M@Ge_{10}]^{2-}$, M = Ni, Pd, Pt are best formulated as containing dianionic M^{2-} endohedral metals ($d^{10}s^2$ configuration) inside a neutral Ge_{10} cage – *i.e.* the metal acts as a net 2-electron acceptor from the cage. The switch in structural preference from D_{4d} for Ni to D_{5h} for Pd and Pt was then rationalised in terms of the difference in volume of the two cages: the smaller deltahedral cage can accommodate the 3d metal but not its 4d and 5d congeners.[18a,b] An alternative perspective is offered by the analysis of the electron density in $[Co@Ge_{10}]^{3-}$ by Fässler and co-workers, which indicates a highly delocalised picture of bonding, leading the authors to conclude that the cluster is best described as an intermetalloid.[17] The transition from an approximately spherical deltahedral structure ($[Ni@Pb_{10}]^{2-}$) to a more open structure for an isoelectronic earlier transition metal analogue ($[Co@Ge_{10}]^{3-}$) is, however, strikingly reminiscent of the $Ni@Pb_{12}$/$[Mn@Pb_{12}]^{3-}$ comparison noted above,[6] where the former is almost perfectly deltahedral while the latter is strongly distorted. By analogy, it seems possible that the adoption of the pentagonal prismatic structures may also be driven by substantial backbonding from the metal to the cluster cage. In this context we note Korber's prescient comment that, "some kind of border seems to have been crossed when moving from Group 10 to Group 9 endohedral atoms, and the encapsulated transition metal atom clearly is not as innocent a template as it was assumed to be from the earlier results".[19]

In this paper we first report the synthesis of a new member of the $M@E_{10}$ family, $[Fe@Sn_{10}]^{3-}$, isolated as its $[K(2,2,2-crypt)]$ salt. This 51-electron cluster, isoelectronic with $[Fe@Ge_{10}]^{3-}$, has been characterised using mass spectrometry and elemental analysis but, frustratingly, we have been unable to obtain high-quality diffraction data. Thus the precise 3-dimensional arrangement of atoms in space and hence the position of the cluster within the spectrum of structural types exhibited by the $M@E_{10}$ family remains unknown. Based on simple electron counting, we might anticipate that 51-electron $[Fe@Sn_{10}]^{3-}$ should exhibit properties intermediate between 52-electron $[Ni@Pb_{10}]^{2-}$ and 50-electron $[Zn@In_{10}]^{8-}$. The dangers of relying on electron count alone are, however, amply demonstrated by the gross differences between isoelectronic members of the family, for example 52-electron $[Ni@Pb_{10}]^{2-}$ and $[Co@Ge_{10}]^{3-}$. In order to resolve these issues we use DFT as a platform to construct a bonding model that encompasses all of the known structural types within the $M@E_{10}$ family (*viz* bicapped square antiprismatic ($[Ni@Pb_{10}]^{2-}$, $[Zn@In_{10}]^{8-}$), tetra-capped trigonal prismatic ($[Ni@In_{10}]^{10-}$) and the pentagonal prismatic $[Fe@Ge_{10}]^{3-}$ and $[Co@Ge_{10}]^{3-}$). The electronic structure of all three classes has been discussed in isolation previously, but here we attempt to link them in a periodic context. The structural chemistry can be rationalised in terms of a continuum defined by the *effective* electron count at the E_{10} cage, which increases in the order $[Zn@In_{10}]^{8-} <$

$[Ni@Pb_{10}]^{2-} \approx 42 < [Fe@Ge_{10}]^{3-}$, rather than the total valence electron count which varies as $[Zn@In_{10}]^{8-} < [Fe@Ge_{10}]^{3-} < [Ni@Pb_{10}]^{2-}$. The emphasis on effective electron count at the cage takes into account the increasingly active nature of the 3d orbitals in the earlier transition metals.

Results and discussion

Synthesis and characterisation of $[Fe@Sn_{10}]^{3-}$

Dissolution of a source of the Sn_9^{4-} anion, K_4Sn_9, and 2,2,2-crypt in ethylenediamine followed by introduction of $Fe_2(Mes)_4$ led to the formation of black crystals of **1**, $[K(2,2,2-crypt)]_3[Fe@Sn_{10}]$. The $[Fe@Sn_{10}]^{3-}$ cluster has a total valence electron count of 51 and is therefore paramagnetic, precluding the collection of $^{117/119}Sn$ NMR spectra for **1**. Despite this limitation the presence of the cluster anion in solution was confirmed by electrospray mass-spectrometry (ESI-MS): the negative ion mode spectrum showed evidence of peaks arising from clusters with lower negative charges, a result of the oxidation of the parent polyanion during the course of the experiment. There is also evidence of ion pairing between anions and charge balancing cations. The negative ion mode spectra of DMF solutions of **1** revealed mass peaks arising from $[Fe@Sn_{10}]^-$ (m/z = 1242.8), $\{[K(2,2,2-crypt)][Fe@Sn_{10}]\}^-$ (m/z = 1659.1) and $\{[K(2,2,2-crypt)]_2[Fe@Sn_{10}]\}^-$ (m/z = 2075.4). There was also evidence of the same mass-envelopes without an interstitial iron atom. The positive ion mode spectrum of the sample revealed a peak corresponding to $\{[K(2,2,2-crypt)]_4[Fe@Sn_{10}]\}^+$ at m/z = 2904.9. Selected mass-envelopes are pictured in Fig. 2. Despite numerous attempts, interpretation of the diffraction data is compromised by disorder problems. A detailed account of our attempts to establish the geometry of the cluster from the diffraction data is included in ESI,† but we conclude that its precise structure remains unknown, as does its place within the context of the known structural chemistry of the $M@E_{10}$ family.
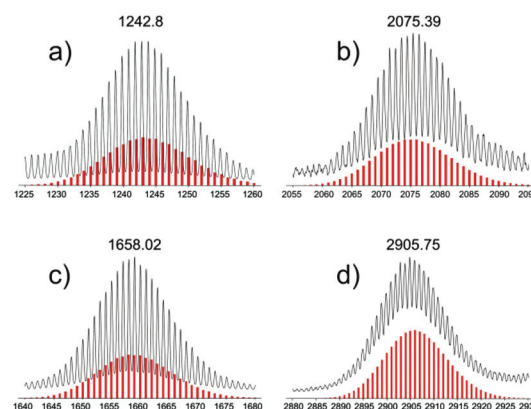

Fig. 2 Selected electrospray mass-envelopes arising from a DMF solution of **1**: (a) $[Fe@Sn_{10}]^{3-}$, (b) $\{[K(2,2,2-crypt)][Fe@Sn_{10}]\}^-$, (c) $\{[K(2,2,2-crypt)]_2[Fe@Sn_{10}]\}^-$ and (d) $\{[K(2,2,2-crypt)]_4[Fe@Sn_{10}]\}^+$. Recorded experimental data are given in black with the calculated isotopic distributions in red.

Electronic structure analysis of the limiting forms of the $M@E_{10}$ family

In this section we first discuss the electronic structure of the prototype members of the $M@E_{10}$ family, *viz* $[Ni@Pb_{10}]^{2-}$, $[Zn@In_{10}]^{8-}$ and $[Fe@Ge_{10}]^{3-}$, the aim being to establish how the structural trends emerge as a natural consequence of periodic variations in the relative energies of the metal and cage orbitals. We then consider the $[Fe@Sn_{10}]^{3-}$ cluster and place it in the context of the known members of the family.

The *closo* deltahedral limit: electronic structure of $[Ni@Pb_{10}]^{2-}$

Computational studies of $[Ni@Pb_{10}]^{2-}$ and its isoelectronic relatives have been reported previously,[11,20] but its central position in the subsequent discussion of less symmetric analogues warrants a review of the key features of the molecular orbital array. The relative energies of key stationary points on the potential energy surface of this and other clusters discussed below are collected in Table 2. Full structural details of the minima are collected in the ESI, Tables S1–4.† The numbering scheme for the atoms used in Tables S1–4† is shown in Fig. 3. At the level of theory used here, the global minimum is indeed the D_{4d}-symmetric structure (Table 2), a bicapped square antiprism with Ni–Pb bond lengths of 3.40 Å (apical) and 2.77 Å (equatorial), very similar to those reported by Chen *et al.*[11] Alternative structures with D_{5h}, C_{3v} and C_{2v} symmetry lie more than 0.5 eV higher in energy. The Ni–Pb distances in the D_{4d}-symmetric minimum are somewhat longer than in the crystal structure, but very similar to those in the empty $[Pb_{10}]^{2-}$ cage optimised at the same level of theory, (3.38 Å, 2.73 Å), confirming that the presence of the metal has minimal impact on the structure of the cage. The molecular orbital array in Fig. 4 (centre) shows the Ni 3d character localised primarily in the upper $\{10a_1, 10e_2, 9e_3\}$ manifold, although mixing with the occupied cage orbitals is apparent in the presence of significant Ni 3d character in the lower-lying $\{9a_1, 8e_3, 9e_2\}$ set as well. Both sets of orbitals are fully occupied, so the distribution of metal and cage character between them does not influence the overall charge distribution. The LUMO, $10e_3$, lies more than 1 eV above the HOMO and has negligible metal character, confirming also the absence of significant
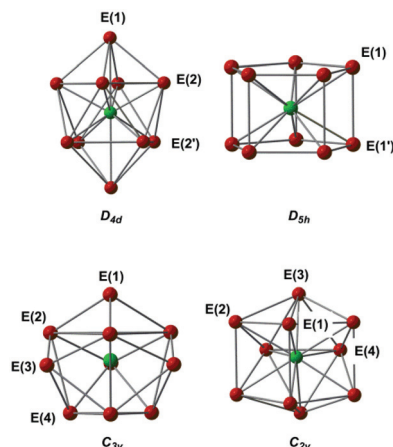

Fig. 3 Structures of various stationary points located on the potential energy surface of $[Ni@Pb_{10}]^{2-}$.

interactions between the filled Ni 3d manifold and the vacant orbitals of the cage (*i.e.* backbonding). In summary, our analysis of the orbital array is entirely consistent with the accepted view that the d^{10} core is structurally inert in this cluster. In such circumstances, the interactions between metal and cluster are mediated by the valence 4s and 4p orbitals on Ni.

Electron deficient 50-electron clusters: $[Ni@In_{10}]^{10-}$ and $[Zn@In_{10}]^{8-}$

The $[Ni@In_{10}]^{10-}$ and $[Zn@In_{10}]^{8-}$ clusters identified by Sevov and Corbett[15] have a formal valence electron count of 50, two fewer than the $[Ni@Pb_{10}]^{2-}$ archetype. The symmetry of the Zn cluster was identified as D_{4d} while the $[Ni@In_{10}]^{10-}$ unit was described as C_{3v} symmetric, based on a tetra-capped trigonal prism. Our own survey of the potential energy surface for $[Zn@In_{10}]^{8-}$ indicates that D_{4d}- and C_{3v}-symmetric minima lie within 0.01 eV of each other (Tables 2 and S2†). Thus the preference for D_{4d} in the Zn case and C_{3v} in the Ni analogue may reflect the presence of 8 and 10 K^+ ions in the lattice, respectively, rather than any intrinsic energetic preference for one structure over the other. Compared to $[Ni@Pb_{10}]^{2-}$, the bicapped square antiprism in $[Zn@In_{10}]^{8-}$ is compressed along the 4-fold axis such that the apical and equatorial vertices are now equidistant from the metal centre (2.87 Å *cf.* 2.81 Å and 2.84 Å in the X-ray structure). The molecular orbital array shown in Fig. 4 indicates that the lower effective nuclear charge of In *vs.* Pb causes a bulk destabilisation of the cage orbitals relative to metal 3d, to the extent that the HOMOs of $[Zn@In_{10}]^{8-}$ are now almost entirely localised on the cluster. The Zn 3d character, in contrast, accumulates in the lower $\{7a_1, 7e_3, 8e_2\}$ band, more than 6 eV below the HOMO. The extended Hückel calculations reported in Sevov and Corbett's original work suggested that the axial compression of the bicapped square antiprism is driven by the need to destabilise the single orbital that becomes vacant when the total valence electron count is reduced from 52 ($[Ni@Pb_{10}]^{2-}$) to 50 ($[Zn@In_{10}]^{8-}$). Our DFT calculations concur entirely with this model: the $10a_1$ orbital, the LUMO $[Zn@In_{10}]^{8-}$, is localised

Table 2 Energies (eV), values of $<S^2>$ and spin densities ($\rho_{\alpha-\beta}$) of stationary points of $[Ni@Pb_{10}]^{2-}$, $[Zn@In_{10}]^{8-}$, $[Fe@Ge_{10}]^{3-}$ and $[Fe@Sn_{10}]^{3-}$. Multiplicities of the states are shown in parentheses

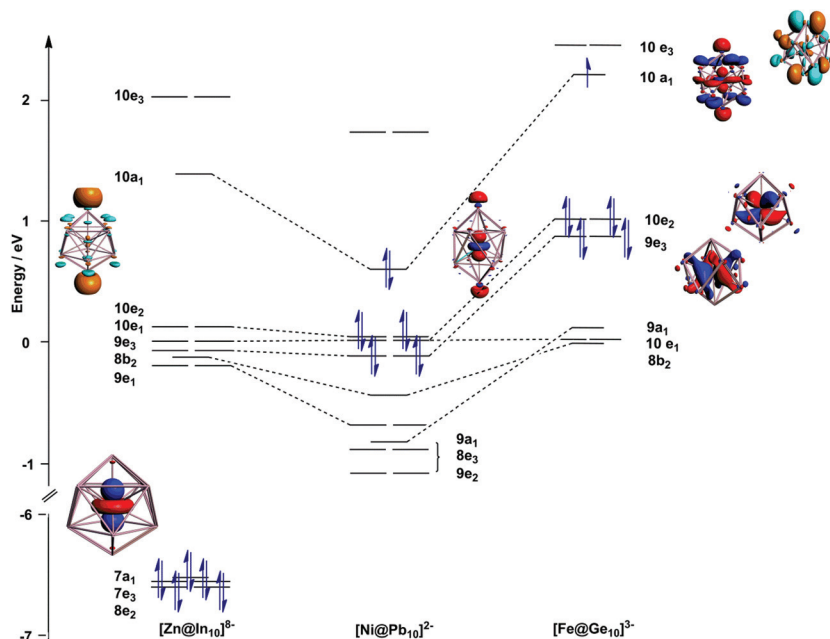|		D_{4d}	C_{3v}	C_{2v}	D_{5h}
$[Ni@Pb_{10}]^{2-}$	Energy $(2S+1)$	0.0 (1)	0.75 (3)	0.53 (1)	2.09 (1)
$[Zn@In_{10}]^{8-}$	Energy $(2S+1)$	0.0 (1)	0.01 (1)		
$[Fe@Ge_{10}]^{3-}$	Energy $(2S+1)$	0.37 (2)	0.35 (2)	+0.26 (2)	0.0 (2)
	$<S^2>$	0.77	0.76	0.77	0.84
	$\rho_{\alpha-\beta}(Fe)$	0.65	0.36	0.53	1.45
	$\rho_{\alpha-\beta}(Ge_{10})$	0.35	0.64	0.47	−0.45
$[Fe@Sn_{10}]^{3-}$	Energy $(2S+1)$	+0.03 (2)	+0.15 (2)	+0.03 (2)	+0.32 (2)
	$<S^2>$	0.80	1.00	0.94	1.09
	$\rho_{\alpha-\beta}(Fe)$	1.16	1.08	1.22	1.96
	$\rho_{\alpha-\beta}(Sn_{10})$	−0.16	−0.08	−0.22	−0.96

Fig. 4 Frontier molecular orbital array of D_{4d}-symmetric isomers of $[Ni@Pb_{10}]^{2-}$, $[Zn@In_{10}]^{8-}$ and $[Fe@Ge_{10}]^{3-}$. Primarily metal-based electrons are shown in blue. The different charges on the clusters mean that the absolute values of the Kohn–Sham eigenvalues are not directly comparable. The $10e_1$ orbital, which has no metal 3d character, is taken as a common reference point for the three diagrams.

predominantly on the cage and moreover has π bonding character around the square faces. Thus it is destabilised by an expansion of these faces which in turn drives a compression along the 4-fold axis (compared to the $[Ni@Pb_{10}]^{2-}$ reference). The inertness of the metal d orbitals is further emphasised by the striking resemblance of the optimised structure of the D_{4d}-symmetric $[Zn@In_{10}]^{8-}$ cluster to that of the empty $[In_{10}]^{10-}$ cage and *not* the more reduced $[In_{10}]^{12-}$ or $[In_{10}]^{14-}$ (ESI, Table S5†). For example, the similarity in Zn–In distances (2.87 Å for both apical and equatorial atoms) is highly characteristic of 40-electron $[In_{10}]^{10-}$ (X–In = 2.80 and 2.75 Å) and not $[In_{10}]^{12-}$ (3.25 and 2.64 Å) or $[In_{10}]^{14-}$ (3.60 and 2.61 Å).

Electronic structure of 51-electron $[Fe@Ge_{10}]^{3-}$

The doublet potential energy surface of $[Fe@Ge_{10}]^{3-}$ again features D_{4d}, C_{3v}, C_{2v} and D_{5h}-symmetric stationary points (Tables 2 and S3†), the global minimum proving to be a D_{5h}-symmetric $^2A_1'$ state. The calculated structural parameters are in excellent agreement with their crystallographic counterparts, precisely as reported by both Fässler and King.[17,18] Amongst the alternative structural motifs, the bicapped square antiprism (D_{4d}, $^2A_1$) lies 0.36 eV above the ground state but is not a true minimum, having one doubly degenerate imaginary frequency. This mode leads to a C_{2v}-symmetric structure with two square face faces which lies 0.26 eV above the $^2A_1'$ global minimum.

Despite the fact that the D_{4d}-symmetric structure is not the global minimum in this case, it provides a convenient point of reference for the comparison between $[Fe@Ge_{10}]^{3-}$, $[Ni@Pb_{10}]^{2-}$ and $[Zn@In_{10}]^{8-}$, the latter two having D_{4d}-symmetric global minima. We noted above that the transition from $[Ni@Pb_{10}]^{2-}$ to $[Zn@In_{10}]^{8-}$ results in a stabilisation of the metal-based

orbitals relative to those on the cage. Precisely the opposite is true if we compare $[Ni@Pb_{10}]^{2-}$ and $[Fe@Ge_{10}]^{3-}$ (Fig. 4): a bulk upward shift in the 3d orbitals caused by the reduced effective nuclear charge at Fe(−I) *vs.* Ni(0) localises the metal 3d character in the upper orbitals, {$10a_1$, $10e_2$, $9e_3$}. When viewed as a continuum, the complete series $[Zn@In_{10}]^{8-} \rightarrow [Ni@Pb_{10}]^{2-} \rightarrow [Fe@Ge_{10}]^{3-}$ is characterised by an upward shift of the metal based orbitals relative to those of the cage, such that whilst they can reasonably be assumed to be structurally inert in both $[Zn@In_{10}]^{8-}$ and $[Ni@Pb_{10}]^{2-}$, the same cannot be said for $[Fe@Ge_{10}]^{3-}$.

The transition from the bicapped square antiprism to the pentagonal prism can be analysed, at least conceptually, *via* a reaction coordinate with a conserved C_2 axis that passes through the C_{2v}-symmetric structure (Scheme 1). In the first step, rotation of a pair of bonded vertices (green in Scheme 1) on opposite sides of the equator of the bicapped square antiprism converts it to the C_{2v}-symmetric intermediate with two square faces. Rotation of the face containing red and blue atoms in Scheme 1 about the same C_2 axis, along with elongation of the edge connecting the two blue vertices, then links the C_{2v}-symmetric intermediate to the pentagonal prism. The
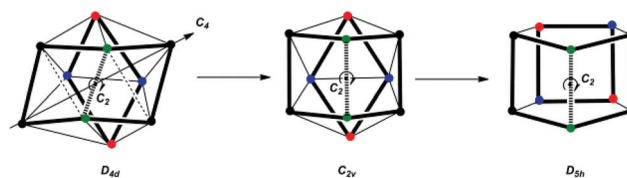
Scheme 1 Hypothetical reaction coordinate connecting the D_{4d} and D_{5h}-symmetric structures *via* the C_{2v}-symmetric intermediate.

transition from triangular to square faces in clusters is generally characteristic of an increased electron count, so the reaction coordinate maps a progressive increase in electron density at the cage.

The correlation of the frontier molecular orbitals across this coordinate is mapped in Fig. 5. The transition from D_{4d} to D_{5h} symmetries via C_{2v} results in a progressive stabilisation of the metal-based orbitals, the root cause of which is enhanced backbonding from the metal 3d into the vacant orbitals of the cage. Thus the $8e_2'/7e_1''$ and $9e_2'/8e_1''$ pairs in the pentagonal prism are the in/out-of-phase combinations of occupied Fe 3d and vacant cage orbitals. Where backbonding occurs in a non-singlet state such as $[Fe@Ge_{10}]^{3-}$, it is necessarily amplified in the spin-β manifold simply because the metal-based spin-β orbitals are higher in energy than their spin-α counterparts due to the effects of spin polarisation. The accumulation of spin-β density on the cage is therefore a clear fingerprint of backbonding. In Table 2 a comparison of the spin densities in the D_{5h}- and D_{4d}-symmetric isomers ($\rho(Fe) = 1.45$ and $\rho(Ge_{10}) = -0.45$ in the former, $\rho(Fe) = 0.65$ and $\rho(Ge_{10}) = 0.35$ in the latter) indicates greatly enhanced backbonding in the pentagonal prism. Whilst the assignment of formal oxidation states in these endohedral clusters is very difficult, the limiting formulations for the cluster are useful to frame the discussion. In the extreme limit of backbonding where all eight electrons in the $8e_2'/7e_1''$ pair are assigned to the cage rather than to the metal, an $[Fe^{7+}@Ge_{10}{}^{10-}]^{3-}$ formulation of the cluster emerges. If, in contrast, only the four higher-lying spin-β electrons are awarded to the cage, this leads to an $[Fe^{3+}@Ge_{10}{}^{6-}]^{3-}$ formulation with the central Fe in an $S = 5/2$ state, antiferromagnetically coupled to a cage carrying four unpaired spin-β electrons. Such high degrees of charge separation are clearly unrealistic, but the emergence of negative spin density on the cage is nevertheless indicative of a shift towards the $[Fe^{3+}@Ge_{10}{}^{6-}]^{3-}$ limit. It is no coincidence that the pentagonal prism, with its

3-connected vertices, is the most stable structure for the known electron precise (50-electron) cluster $Sn_{10}R_{10}$, R = 2,6-$Et_2C_6H_3$),[21] isoelectronic with $[Ge_{10}]^{10-}$. The preference for bicapped square antiprismatic geometries for empty 42-electron clusters ($[Pb_{10}]^{2-}$) but pentagonal prismatic geometries for empty 50-electron analogues arises because the $D_{4d} \rightarrow D_{5h}$ structural distortion stabilises four vacant orbitals on the 42-electron cage, precisely the number required to accommodate the four additional pairs of electrons in $[E_{10}]^{10-}$ or the four additional unpaired electrons in $[E_{10}]^{6-}$.[22] The isomorphism between $[Fe@Ge_{10}]^{3-}$ and the empty $[Ge_{10}]^{10-}$ cage arises because any substantial degree of backbonding involving four orthogonal d orbitals ($8e_2'/7e_1''$ in this case) places exactly the same structural demands on the cluster as a complete eight-electron reduction would: a rearrangement that stabilises precisely four vacant orbitals on the cage will be favoured. Thus in endohedral clusters where the metal d orbitals are not inert, the structural preferences are controlled *not* by the total amount of electron density transferred to the cage, but rather by the number of metal d orbitals that participate in the backbonding. We have emphasised the significance of backbonding from *four* distinct 3d orbitals on Fe, so it is important to consider why the fifth is not also involved, as this should, in principle, drive a distortion to a different structure, isomorphic with $[Ge_{10}]^{12-}$ rather than $[Ge_{10}]^{10-}$. The SOMO of the D_{5h} symmetric cluster is the $8a_1'$ orbital, primarily of Fe d_{z^2} character, directed towards the centre of the pentagonal faces. The lack of substantial overlap means that backbonding is minimal, despite the high energy of this orbital. The absence of a structural role for the singly occupied $8a_1'$ orbital in 51-electron $[Fe@Ge_{10}]^{3-}$ explains why it is isostructural with 52-electron $[Co@Ge_{10}]^{3-}$ where the same orbital is doubly occupied. We also note here that our assignment of a $^2A_1'$ ground state contrasts with the $^2E_2''$ proposed by King and co-workers,[18] where the vacancy lies in the cage-based $8e_2''$ rather
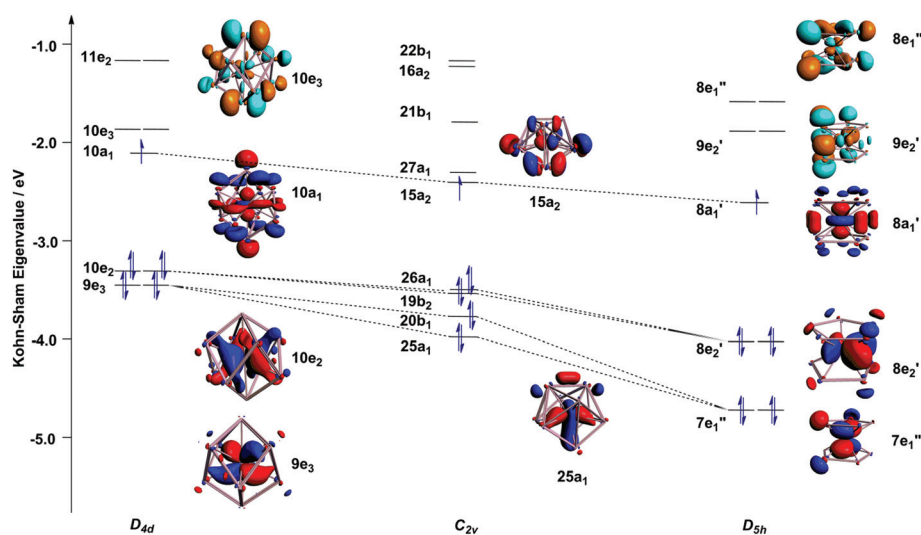

Fig. 5 Evolution of the Kohn–Sham orbitals (only spin-β are shown) of $[Fe@Ge_{10}]^{3-}$ along the C_2-symmetric coordinate linking the D_{4d}-, C_{2v}- and D_{5h}-symmetric minima. Dashed lines trace the primarily metal-based orbitals. Full MO diagrams showing both spin-α and spin-β manifolds are collected in ESI, Fig. S3.†
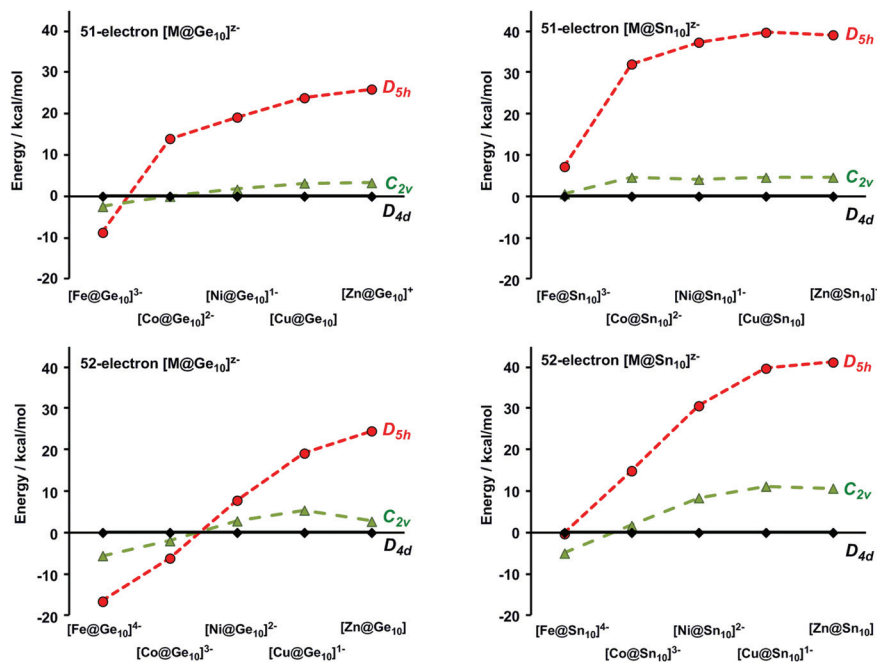
Fig. 6 Relative energies of the D_{5h}-, D_{4d}- and C_{2v}-symmetric isomers for isoelectronic $[M@E_{10}]^n$ (M = Fe, Co, Ni, Cu, Zn) series. In all cases the bicapped square anti-prismatic structure (D_{4d}) is taken as the energetic reference.

than $8a_1'$. At our chosen level of theory the $^2E''_2$ state lies 0.74 eV above $^2A_1'$ due to the combined effects of reduced effective nuclear charge and spin polarization at the Fe centre. Unlike the $^2E''_2$ alternative, our $^2A_1'$ ground state is fully consistent with the rigorously D_{5h}-symmetric structure of $[Fe@Ge_{10}]^{3-}.^{2c}$

The reaction coordinate shown in Scheme 1 suggests that the C_{2v}-symmetric structure is, in structural terms, intermediate between D_{4d} and D_{5h} limits, with two square faces (*vs.* none in D_{4d} and five in D_{5h}). The frontier orbitals in Fig. 5 confirm that it is also intermediate in an electronic sense, with the metal manifold (and specifically the $20b_1$ and $25a_1$ orbitals) stabilised relative to the D_{4d} case, but not to the same extent as the D_{5h} limit. The transition from D_{4d} to C_{2v} therefore enhances back-bonding from only two of the five metal 3d orbitals, and is therefore less effective in relieving the high electron density at the metal than complete rearrangement to a pentagonal prism.

A continuum model for M@E$_{10}$ clusters and predictions for [Fe@Sn$_{10}$]$^{3-}$

The arguments set out in the preceding paragraphs identify the interaction between an electron-rich early to mid transition metal and the vacant orbitals of the cage as the dominant driving force for distortion away from an ideal bicapped square antiprismatic structure such as that adopted by $[Ni@Pb_{10}]^{2-}$. A broader survey of isoelectronic 51- and 52-electron clusters, $[M@Ge_{10}]^n$ and $[M@Sn_{10}]^n$ and (M = Fe, Co, Ni, Cu, Zn) (Fig. 6), establishes a clear trend towards stabilisation of the D_{5h}-symmetric structure relative to D_{4d} in the earlier transition elements, where the metal is more electropositive. At the 52-electron level the crossover for M@Ge$_{10}$ does indeed occur between Groups 10 and 9, as anticipated by Korber,[19]

while at the 51-electron level a more electropositive metal is required, displacing the crossover one position to the left. Although less dramatic than the D_{5h}/D_{4d} comparison, a distinct stabilisation of the C_{2v}-symmetric structure relative to D_{4d} is also apparent for the earlier elements, confirming the intermediate position of the latter in Scheme 1.

The $[Fe@Sn_{10}]^{3-}$ cluster anion is of particular interest as it provided the initial motivation for our computational investigation, and Fig. 6 confirms that similar periodic trends emerge in the M@Ge$_{10}$ and M@Sn$_{10}$ family. The D_{5h}-symmetric structures are, however, systematically destabilised relative to D_{4d} or C_{2v} for M@Sn$_{10}$ clusters, such that they are never the global minimum. $[Fe@Sn_{10}]^{3-}$ is therefore unique among the 51-electron clusters in so much as the C_{2v}-symmetric and D_{4d}-symmetric structures are almost isoenergetic yet *both* are still more stable than the pentagonal prism. In fact neither of the D_{4d}- or C_{2v}-symmetric structures are true minima, the most stable point on the surface being an intermediate C_2-symmetric structure where the Sn–Sn bond bridging the square faces (shown in green in Scheme 1) is only partially rotated about the C_2 axis (structure shown in ESI, Fig. S4†).§ The D_{4d}-, C_{2v}- and C_2-symmetric structures are, however, separated by less than 0.03 eV, and we cannot identify the global minimum with confidence, other than to note that it is lies somewhere along a very flat potential energy surface defined by the reaction coordinate in Scheme 1. In the context of the Bürgi–Dunitz structural

§This C_2-symmetric minimum appears to be unique to the $[Fe@Sn_{10}]^{3-}$ cluster where the D_{4d} and C_{2v}-symmetric structures that it connects are almost degenerate. In all other cases that we have considered, similar C_2-symmetric structures collapse to either D_{4d} or C_{2v}, whichever is the more stable.

correlation model,[23] the flatness of the potential energy surface should result in substantial deformations of the cluster in response to environmental effects such as change in cation or temperature. Indeed, the intrinsic flexibility of the cluster may contribute to the difficulties experienced in refining the crystallographic data. What is abundantly clear, however, is that it is *not* pentagonal prismatic like its isoelectronic congener $[Fe@Ge_{10}]^{3-}$, nor is it rigidly bicapped square antiprismatic like 52-electron $[Ni@Pb_{10}]^{2-}$. There is a superficial resemblance to the structural chemistry of $[Zn@In_{10}]^{8-}$ and $[Ni@In_{10}]^{10-}$, in so much as all three clusters have low-lying stationary points with C_{3v}, C_{2v} and D_{4d} symmetry. Given that we invoke effective cage electron counts in excess of 42 as the driving force for distortion in $[Fe@Sn_{10}]^{3-}$ but counts of less than 42 in $[Zn@In_{10}]^{8-}$ and $[Ni@In_{10}]^{10-}$, this apparent similarity merits further comment. We noted previously in reference to Tables 2 and S5† that the In_{10} cages in the D_{4d}-symmetric isomer of $[Zn@In_{10}]^{8-}$ resembles 40-electron $[In_{10}]^{10-}$ rather more closely than 42-electron $[In_{10}]^{12-}$ or 44-electron $[In_{10}]^{14-}$. In the $[Fe@Sn_{10}]^{3-}$ case the situation is precisely the opposite: the optimised D_{4d}-symmetric structure bears a closer resemblance to 42- and 44-electron $[Sn_{10}]^{2-}$ and $[Sn_{10}]^{4-}$ than it does to 40-electron $[Sn_{10}]^{0}$ (ESI, Table S5†), most strikingly in the prolate distortion (Fe–Sn apical > Fe–Sn equatorial) that is highly characteristic of effective cage electron counts of 42 or more. Thus the symmetry of a distorted cluster alone is not necessarily indicative of the underlying driving force: careful attention must be paid to the precise structural details to distinguish electron rich from electron-deficient cases.

The correlation of frontier orbitals in Fig. 5 shows that distortion from a D_{4d} to a C_{2v}-symmetric structure enhances backbonding from the Fe(–I) center, but is less optimal in this regard than complete rearrangement to the pentagonal prism. So why then does the $[Fe@Sn_{10}]^{3-}$ cluster stop at the C_{2v} structure while $[Fe@Ge_{10}]^{3-}$ goes all the way to the D_{5h} limit? To answer this, we note from the spin densities in Tables 1 and 2 that *only* the pentagonal prism is able to accommodate the significant backbonding needed to stabilise the extremely electron rich Fe(–I) center in $[Fe@Ge_{10}]^{3-}$: in all other geometries the spin density on the Ge_{10} cage is positive. Thus a switch to a prismatic geometry is apparently essential if a Ge_{10} cage is to accommodate the electron density from a very electron-rich endohedral metal. In contrast, $\rho(Sn_{10}) < 0$ for *all* isomers of $[Fe@Sn_{10}]^{3-}$, indicating that backbonding is relatively more effective even in the approximately deltahedral structures (D_{4d}, C_{2v}), albeit to a lesser extent than in the pentagonal prismatic alternative. The enhanced backbonding in the Sn systems stems from the weaker overlap between the 5p orbitals of Sn compared to 4p of Ge, which serves to compress the HOMO–LUMO gap of the Sn_{10} cage, irrespective of its structure.

Conclusions

This work has been motivated by a curiosity about the structure of a new cluster compound, $[Fe@Sn_{10}]^{3-}$, which has been synthesised in our laboratory but has, at least thus far, resisted crystallographic characterisation. We wished to place this new cluster within the context of the known structural chemistry of the diverse $M@E_{10}$ family, which features perfect deltahedra ($[Ni@Pb_{10}]^{2-}$), compressed deltahedra ($[Zn@In_{10}]^{8-}$) and the pentagonal prismatic $[Fe@Ge_{10}]^{3-}$ and $[Co@Ge_{10}]^{3-}$. This in turn has led us to establish links between these apparently very different structural types, which in fact lie on a continuum defined by the *effective* electron density at the cage. This parameter takes into account the increasingly active role of the d orbitals to the left of the transition series, and increases in the order $[Ni@In_{10}]^{10-} < [Ni@Pb_{10}]^{2-} < [Fe@Ge_{10}]^{3-}$. The adoption of a D_{5h} symmetric structure is indicative of substantial backbonding from the metal (formally Fe(–I) or Co(–I)) to the cage but the structural preference is determined *not* by the total amount of electron density transferred to the cage (which is small) but rather by the *number of orthogonal metal* d *orbitals* that participate in the backbonding. Thus D_{5h}-symmetric $[Fe@Ge_{10}]^{3-}$ and $[Co@Ge_{10}]^{3-}$, where *four* d orbitals participate in backbonding, are isostructural with the electron-precise 50-electron $Sn_{10}(2,6-Et_2C_6H_3)_{10}$ which has *four* additional pairs of electrons compared to the *closo* reference point, 42-electron $[Ge_{10}]^{2-}$. Our model differs somewhat from that put forward by King and co-workers, who have proposed that the structural chemistry is controlled by size, the larger metal ions preferring the larger pentagonal prism.[18] It is difficult to separate these two arguments because the size of a metal ion and its ability to participate in backbonding are intimately related, both being consequences of variation in effective nuclear charge. Nevertheless, it is clear from our calculations and those of others[17] that the orbitals of the cage are far from innocent in the D_{5h} structure. Our survey also suggest that the global minimum for the $[Fe@Sn_{10}]^{3-}$ anion is very different to isoelectronic $[Fe@Ge_{10}]^{3-}$, and sits on a flat potential energy surface connecting D_{4d}, C_{3v} and C_{2v}-symmetric structures. The different structural preferences can be traced to the greater ability of the Sn_{10} cage to accommodate electron density, which means that the high electron density on the formally Fe(–I) centre can be relieved without the need for extreme distortion represented by the pentagonal prismatic geometry. The new $[Fe@Sn_{10}]^{3-}$ anion therefore represents a point intermediate between $[Ni@Pb_{10}]^{2-}$ and $[Fe@Ge_{10}]^{3-}$ in the $M@E_{10}$ family.

Experimental procedures

Computational methods

All calculations described in this paper were performed with the Amsterdam Density Functional package (ADF2010.02).[24] The TZ2P Slater-type basis set of triple-ζ quality, extended with two polarisation functions, was used to describe the 1st row transition metals (M = Fe, Co, Ni, Cu, Zn) as well as the Group 13 and 14 elements (E = In, Ge, Sn). Electrons in orbitals up to and including 2p for the transition metals, 3p on Ge, 4d on In and Sn and 5d on Pb were considered part of the core and

treated in accordance with the frozen core approximation (M.2p, Ge.3p, Sn.4d, In.4d, Pb.5d). All calculations employed the Local Density Approximation (LDA) to the exchange potential,[25] along with the local exchange-correlation potential of Vosko, Wilk and Nusair (VWN)[26] and gradient corrections to non-local exchange and correlation proposed by Becke and Perdew (BP86).[27] All calculations were unrestricted. Relativistic effects were incorporated using the Zeroth Order Relativistic Approximation (ZORA).[28] The confining effect of cations in the crystal lattice was modeled by surrounding the clusters with a continuum dielectric model (COSMO).[29] The chosen dielectric constant $\varepsilon = 78.4$ corresponds to that of water although structural parameters are not strongly dependent on this choice. All structures were optimised using the gradient algorithm of Versluis and Ziegler.[30] During the initial geometry optimisation of the clusters the symmetries were kept fixed. When imaginary frequencies were present in the converged structure further optimisation using structures distorted along the imaginary modes lead to the nearest local minimum.

General synthetic methods

All reactions and product manipulations were carried out under an inert atmosphere using standard Schlenk-line or glovebox techniques (MBraun UNILab glovebox maintained at <0.1 ppm H_2O and <0.1 ppm O_2). The intermetallic precursor K_4Sn_9 was synthesised according to a previously reported synthetic procedure from a stoichiometric mixture of the elements (K: 99.95%, Aldrich; Sn: 99.8%, Strem).[31] $Fe_2(Mes)_4$ was synthesised using a literature-reported method.[32] 2,2,2-Crypt (4,7,13,16,21,24-hexaoxa-1,10-diazabicyclo[8.8.8]hexacosane; 99+%, Merck) was used as received after careful drying under vacuum. Tetrahydrofuran (THF; 99.9%, Rathburn), toluene (tol; 99.9%, Rathburn) and dimethylformamide (DMF; 99.9%, Rathburn) were purified using an MBraun SPS-800 solvent system. Ethylenediamine (en; 99%, Aldrich) was distilled over sodium metal. All solvents were stored under argon in gas-tight ampoules. In addition THF and Et_2O were stored over activated 3 Å molecular sieves (Acros).

Synthesis of $[K(2,2,2\text{-crypt})]_3[Fe@Sn_{10}]\cdot4C_5H_5N$ (1)

K_4Sn_9 (90 mg, 0.073 mmol) and 2,2,2-crypt (100 mg, 0.266 mmol) were dissolved in ethylenediamine (2 mL) yielding a dark brown solution. In a separate reaction vessel, $Fe_2(Mes)_4$ (22 mg, 0.037 mmol) was dissolved in THF (2 mL) to give a reddish-brown solution. The THF solution was added dropwise to the stirred ethylenediamine solution and the reaction mixture stirred for 1 h, filtered and reduced to dryness under vacuum. The resulting solid was redissolved in pyridine (2 mL) yielding a dark brown solution. This solution was filtered into a crystallisation ampoule and layered with toluene. After several days, black rod-like crystals of **1** were obtained alongside some metallic decomposition. Due to the low crystalline yield of this synthetic method, a slightly modified bulk synthesis of **1** was developed. K_4Sn_9 (203 mg, 0.166 mmol) and 2,2,2-crypt (250 mg, 0.664 mmol) were dissolved in ethylenediamine (4 mL) to give a dark brown solution. The mixture was

allowed to stir for 1 h after which toluene (40 mL) was added. Stirring for 30 minutes yielded a black precipitate which was left to stand for an additional half an hour. The colourless solution was filtered off and the solid precipitate dried *in vacuo*. The resulting dark red/black powder (360 mg, 79%) was isolated in the glovebox. Assuming the product has the formula $[K(2,2,2\text{-crypt})]_4[Sn_9]$, some of the dark red/black powder (180 mg, 0.066 mmol) was dissolved in pyridine (2 mL) to give a dark brown solution. $Fe_2(Mes)_4$ (29 mg, 0.049 mmol) was dissolved in THF (2 mL) to give a brown solution. The THF solution was added dropwise to the stirred pyridine solution. The reaction mixture was stirred for 1 h and toluene (40 mL) added to give black precipitate. The mixture was then stirred for 30 minutes and left to stand. The pale yellow solution was filtered off and the solid precipitate dried under a dynamic vacuum for half an hour. A black powder sample of **1** (140 mg, 68%) was isolated in the glovebox. Anal. Calcd for $C_{74}H_{128}FeK_3N_{10}O_{18}Sn_{10}$: C 31.66, H 4.60, N 4.99. Found: C 31.49, H 4.48, N 4.81. ESI-MS (−): m/z 1187.0 $[Sn_{10}]^-$, 1242.8 $[Fe@Sn_{10}]^-$, 1602.3 $\{[K(2,2,2\text{-crypt})][Sn_{10}]\}^-$, 1659.1 $\{[K(2,2,2\text{-crypt})][Fe@Sn_{10}]\}^-$, 2019.5 $\{[K(2,2,2\text{-crypt})]_2[Sn_{10}]\}^-$, 2075.4 $\{[K(2,2,2\text{-crypt})]_2[Fe@Sn_{10}]\}^-$. ESI-MS (+): 2315.0 $\{[K(2,2,2\text{-crypt})]_3[Sn_9]\}^+$, 2433.8 $\{[K(2,2,2\text{-crypt})]_3[Sn_{10}]\}^+$, 2850.1 $\{[K(2,2,2\text{-crypt})]_4[Sn_{10}]\}^+$, 2904.9 $\{[K(2,2,2\text{-crypt})]_4[Fe@Sn_{10}]\}^+$. Positive and negative ion mode electrospray mass spectra (ESI-MS) were recorded from DMF solutions (10–20 μM) on a Masslynx LCT Time of Flight mass spectrometer with a Z-spray source (150 °C source temperature, 200 °C desolvation temperature, 2.4 kV capillary voltage and 25 V cone voltage). The samples were introduced directly with a 1 mL SGE syringe and a syringe pump at 0.6 mL h^{-1}. CHN elemental analyses were performed on 5 mg samples submitted under vacuum in flame-sealed Pyrex ampoules.

Notes and references

1 (*a*) S. Neukermans, E. Janssens, Z. F. Chen, R. E. Silverans, P. von Rague Schleyer and P. Lievens, *Phys. Rev. Lett.*, 2004, **92**, 163401; (*b*) X. Xing, Z. Tian, H. Liu and Z. Tang, *Rapid Commun. Mass Spectrom.*, 2003, **17**, 1411; (*c*) M. Ohara, K. Koyasu, A. Nakajima and K. Kaya, *Chem. Phys. Lett.*, 2003, **371**, 490; (*d*) H. Hiura, T. Miyazaki and T. Kanayama, *Phys. Rev. Lett.*, 2001, **86**, 1733; (*e*) X. Zhang, G. Li, X. Xing, X. Zhao, Z. Tang and Z. Gao, *Rapid Commun. Mass Spectrom.*, 2001, **15**, 2399.

2 For recent reviews see: (a) S. C. Sevov and J. M. Goicoechea, *Organometallics*, 2006, **25**, 5678; (b) S. Scharfe and T. F. Fässler, *Philos. Trans. R. Soc. London, Ser. A*, 2010, **368**, 1265; (c) S. Scharfe, F. Kraus, S. Stegmaier, A. Schier and T. F. Fässler, *Angew. Chem., Int. Ed.*, 2011, **50**, 3630.

3 E. N. Esentürk, J. Fettinger, Y. F. Lam and B. W. Eichhorn, *Angew. Chem., Int. Ed.*, 2004, **43**, 2132.

4 E. N. Esentürk, J. Fettinger and B. W. Eichhorn, *J. Am. Chem. Soc.*, 2006, **128**, 9178.

5 J.-Q. Wang, S. Stegmaier, B. Wahl and T. F. Fässler, *Chem.–Eur. J.*, 2010, **16**, 1793.

6 B. Zhou, T. Krämer, A. L. Thompson, J. E. McGrady and J. M. Goicoechea, *Inorg. Chem.*, 2011, **50**, 8028.

7 (a) K. Wade, *Adv. Inorg. Chem.*, 1976, **18**, 1; (b) K. Wade, *J. Chem. Soc. D*, 1971, 792; (c) D. M. P. Mingos, *Nat. Phys. Sci.*, 1972, **99**, 236; (d) D. M. P. Mingos, *Acc. Chem. Res.*, 1984, **17**, 311.

8 X. Chen, K. Deng, Y. Liu, C. Tang, Y. Yuan, F. Hu, H. Wu, D. Huang, W. Tan and X. Wang, *Chem. Phys. Lett.*, 2008, **462**, 275.

9 E. N. Esentürk, J. Fettinger and B. W. Eichhorn, *Chem. Commun.*, 2005, 247.

10 A. Spiekermann, S. D. Hoffmann and T. F. Fässler, *Angew. Chem., Int. Ed.*, 2006, **45**, 3459.

11 Z. Chen, S. Neukermans, X. Wang, E. Janssens, Z. Zhou, R. E. Silverans, R. B. King, P. von Rague Schleyer and P. Lievens, *J. Am. Chem. Soc.*, 2006, **128**, 12829.

12 (a) J. M. Goicoechea and S. C. Sevov, *J. Am. Chem. Soc.*, 2006, **128**, 4155; (b) D. Rios, M. M. Gillett-Kunnath, J. D. Taylor, A. G. Oliver and S. C. Sevov, *Inorg. Chem.*, 2011, **50**, 2373.

13 D. Rios and S. C. Sevov, *Inorg. Chem.*, 2010, **49**, 6396.

14 (a) J. M. Goicoechea and S. C. Sevov, *Organometallics*, 2006, **25**, 4530; (b) B. Zhou, M. S. Denning, T. A. D. Chapman and J. M. Goicoechea, *Inorg. Chem.*, 2009, **48**, 2899; (c) B. Zhou, M. S. Denning, C. Jones and J. M. Goicoechea, *Dalton Trans.*, 2009, 1571.

15 (a) S. C. Sevov and J. D. Corbett, *Inorg. Chem.*, 1993, **32**, 1059; (b) S. C. Sevov, J. D. Corbett and J. E. Ostenton, *J. Alloys Compd.*, 1993, **202**, 289; (c) S. C. Sevov and J. D. Corbett, *J. Am. Chem. Soc.*, 1993, **115**, 9089.

16 B. Zhou, M. S. Denning, D. L. Kays and J. M. Goicoechea, *J. Am. Chem. Soc.*, 2009, **131**, 2802.

17 J.-Q. Wang, S. Stegmaier and T. F. Fässler, *Angew. Chem., Int. Ed.*, 2009, **48**, 1998.

18 (a) R. B. King, *Struct. Bonding*, 2011, **140**, 1; (b) R. B. King, I. Silaghi-Dumitrescu and M.-M. Uţă, *J. Phys. Chem. A*, 2009, **113**, 527; (c) R. B. King, I. Silaghi-Dumitrescu and M.-M. Uţă, *Chem.–Eur. J.*, 2008, **14**, 4542; (d) R. B. King, I. Silaghi-Dumitrescu and M.-M. Uţă, *J. Phys. Chem. A*, 2011, **115**, 2847.

19 N. Korber, *Angew. Chem., Int. Ed.*, 2009, **48**, 3216.

20 A. Grubisic, H. Wang, X. Li, Y.-J. Ko, F. S. Kocak, M. R. Pedersen, K. H. Bowen and B. W. Eichhorn, *Proc. Natl. Acad. Sci. U. S. A.*, 2011, **108**, 14757.

21 L. R. Sita and I. Kinoshita, *J. Am. Chem. Soc.*, 1991, **113**, 1856.

22 J. E. McGrady, *J. Chem. Educ.*, 2004, **81**, 733.

23 H. B. Bürgi and J. Dunitz, *Structural Correlation*, Wiley, 1994.

24 (a) G. te Velde, F. M. Bickelhaupt, E. J. Baerends, C. Fonseca Guerra, S. J. A. van Gisbergen, J. G. Snijders and T. Ziegler, *J. Comput. Chem.*, 2001, **22**, 931; (b) C. Fonseca Guerra, J. G. Snijders, G. te Velde and E. J. Baerends, *Theor. Chem. Acc.*, 1998, **99**, 391; (c) ADF2010, E. J. Baerends, *et al.*, *SCM, Theoretical Chemistry*, Vrije Universiteit, Amsterdam, The Netherlands, http://www.scm.com

25 R. G. Parr and W. Yang, *Density Functional Theory of Atoms and Molecules*, Oxford University Press, Oxford, 1989.

26 S. H. Vosko, L. Wilk and M. Nusair, *Can. J. Phys.*, 1980, **58**, 1200.

27 (a) A. D. Becke, *Phys. Rev. A: At., Mol., Opt. Phys.*, 1988, **38**, 3098; (b) J. P. Perdew, *Phys. Rev. B*, 1986, **33**, 8822.

28 (a) E. van Lenthe, E. J. Baerends and J. G. Snijders, *J. Chem. Phys.*, 1993, **99**, 4597; (b) E. van Lenthe, E. J. Baerends and J. G. Snijders, *J. Chem. Phys.*, 1994, **101**, 9783; (c) E. van Lenthe, A. E. Ehlers and E. J. Baerends, *J. Chem. Phys.*, 1999, **110**, 8943.

29 A. Klamt, *J. Phys. Chem.*, 1995, **99**, 2224.

30 L. Versluis and T. Ziegler, *J. Chem. Phys.*, 1988, **88**, 322.

31 (a) H. G. von Schnering, M. Baitinger, U. Bolle, W. Carrillo-Cabrera, J. Curda, Y. Grin, F. Heinemann, J. Llanos, K. Peters, A. Schmeding and M. Somer, *Z. Anorg. Allg. Chem.*, 1997, **623**, 1037; (b) C. Hoch, M. Wendorff and C. Röhr, *Acta Crystallogr., Sect. C: Cryst. Struct. Commun.*, 2002, **58**, i45.

32 A. Klose, E. Solari, C. Floriani, A. Chiesi-Villa, C. Rizzoli and N. Re, *J. Am. Chem. Soc.*, 1994, **116**, 9123.